Label free detection of miRNA-21 with Electrolyte Gated Organic Field Effect Transistors (EGOFETs)

Meenu Selvaraj[1,2], Pierpaolo Greco[3*], Matteo Sensi[3], Gulseren Deniz Saygin[1,4], Noemi Bellassai[2], Roberta D'Agata[2], Giuseppe Spoto[2], Fabio Biscarini[3,5*]

[1] Scriba Nanotecnologie s.r.l., Via di Corticella 183/8, I-40128 Bologna, Italy

[2] Department of Chemical Sciences, Università di Catania, Viale Andrea Doria 6, I-95125 Catania, Italy

[3] Department of Life Sciences, Università degli Studi di Modena e Reggio Emilia, Via Campi 103, I-41125 Modena, Italy

[4] Department of Physics, Informatics and Mathematics, Università degli Studi di Modena e Reggio Emilia, Via Campi 103, I-41125 Modena, Italy

[5] Center for Translational Neurophysiology - Istituto Italiano di Tecnologia, Via Fossato di Mortara 17-19, I-44100 Ferrara (Italy)

Corresponding author(s). PG, FB

Abstract:

We report a dual gate/common channel organic transistor architecture designed for quantifying the concentration of one of the strands of miRNA-21 in solution. The device allows one to measure the differential response between two gate electrodes, viz. one sensing and one reference, both immersed in the electrolyte above the transistor channel. Hybridization with oligonucleotide in the picomolar regime induces a sizable reduction of the current flowing through the transistor channel. The device signal is reported at various gate voltages, showing maximum sensitivity in the sublinear regime, with a limit of detection as low as 35 pM. We describe the dose curves with an analytical function derived from a thermodynamic model of the reaction equilibria relevant in our experiment and device configuration, and we show that the apparent Hill dependence on analyte concentration, whose exponent lies between 0.5 and 1, emerges from the interplay of the different equilibria. The binding free energy characteristic of the hybridization on the device surface is found to be

approximately 20% lower with respect to the reaction in solution, hinting to partially inhibiting effect of the surface and presence of competing reactions. Impedance spectroscopy and surface plasmon resonance (SPR) performed on the same oligonucleotide pair were correlated to the electronic current transduced by the EGOFET, and confirmed the selectivity of the biorecognition probe covalently bound on the gold surface.

INTRODUCTION

MicroRNAs (miRNA) are a class of biomarkers whose relevance in oncology is increasing enormously, especially for neuroblastoma and lung cancer (Khalil et al., 2016). Detection of miRNA circulating in blood appears a potential strategy for cancer early diagnosis and patient monitoring (Gasparello et al., 2018), besides providing insights into the cellular path of disease. Since miRNAs with different sequences may act either as tumor promoter or tumor suppressor in the presence of interacting drugs (Gambari et al., 2016), accurate methods for quantification of miRNA are of potential impact for both diagnostics and study of therapeutic efficacy. For these reasons, PCR-assisted low volume analytic protocols, as well as PCR-free isothermal amplification methods, are emerging as new techniques to tackle the difficult task of counting a small number of oligonucleotides in complex matrices (Giuffrida et al., 2015).

Among the numerous miRNAs involved in disease diagnostics and therapy, miRNA-21 is one of the most studied because has been conserved through evolution of vertebrates up to humans and its main biological functions are linked with anti-apoptosis and pro-survival factors (Feng and Tsao, 2016). In the immune system, miRNA-21 has been shown to regulate the gene coding for inflammation biomarker IL-12 (Lu et al., 2009). Temporary silencing of miRNA-21 was correlated with cell differentiation and development in thyroid cells (Landgraf et al., 2007), whereas in the large majority of cancer diseases, miRNA-21 is upregulated. High levels of miRNA-21 were correlated, as promoting progression, with breast cancer (Fang et al., 2017), pancreatic cancer (Qu et al., 2017), lung cancer (Markou et al., 2016), glioblastoma (Luo et al., 2017).

The concentration of oligonucleotides is measured in clinical studies with quantitative PCR. More recently, analytical tools based on PCR-free hybridization in microfluidics appeared, where surface plasmon resonance and droplet based microfluidics are exploited (Bellassai et al., 2019).

Electrochemical methods for miRNA detection were extensively investigated. An example consists of gold nanoparticles functionalized with DNA-bioreceptor and using iridium complexes for redox reactions. This approach yields femtomolar limit of detection (LOD) in controlled hybridization (Miao et al., 2016). Another example features sensing probes, synthetized as complementary strands to the mature miRNA, anchored to a gold electrode surface by means of thiol chemistry (Cardoso et al., 2016), and capable to detect attomolar levels of miRNA-155 (marker of breast cancer).

Optical detection, based on either absorption or fluorescence, requires labelling of the probe with either gold nanoparticles (Hakimian et al., 2018) or fluorescent molecules whose signal changes upon the formation of the duplex (Cadoni et al., 2020). Molecular beacons, consisting of paired fluorophore and quencher (D'Agata and Spoto, 2019), yield a fluorescent label upon the separation of the two parts induced by hybridization.

Label-free biosensors, based on electronic or ionic transport, transduce a specific reaction of the target analyte with a modulation of the charge transport in an inorganic (Majd et al., 2018) or organic semiconductor (Berto et al., 2016) channel, thus changing the current flowing in the channel. Electrolyte gated organic field-effect transistors (EGOFET) are able to quantify ultra-low concentrations of diverse biomarkers (Casalini et al., 2015; Di Lauro et al. 2020; Macchia et al., 2020; Sensi et al., 2020). Moreover, this architecture offers the opportunity to integrate complementary techniques sensitive to biorecognition, such as fluorescence microscopy or surface plasmon resonance (Aspermair et al., 2020). EGOFET enables ultrasensitive detection of antigens because the electrostatic potential of the gate electrode, which is sensitive to antigen binding at surface bound recognition sites, is capacitively coupled to the channel. An amplified shift of the Fermi level of the organic semiconductor is achieved even for low amount of biomolecules adsorbed or grafted on the gate electrode (Berto et al., 2016). Multiple biomarkers detection is possible within the same integrated EGOFET microfluidic device, by miniaturization and multiplexing gate electrodes immersed in the electrolyte solution. Demonstration of multigate architecture was reported by our group for the detection of inflammatory biomarker TNFα using

aptamer functionalization with standard manufacturing processes employed for printed circuit board production. (Parkula et al., 2020).

In the present article, we report the fabrication and assessment of an EGOFET device with dual gate architecture designed for sensing solutions containing a single-stranded segment of miRNA-21 (miRNA-21-3p, also termed target analyte (T), see *Experimental Section*) at concentrations down to tens picomolar range. Our device operates on the differential electronic response of the transistor to the two gate sweeps: one of the gate electrodes, termed G2, is grafted with the complementary sequence bioreceptor (miRNA-21-5p, also termed probe (P)), while the other gate electrode, termed G1, is functionalized with a tightly packed organic monolayer that reduces unspecific adsorption on the Au surface. The G1 electrode serves as an internal reference electrode, whereas the G2 electrode as the sensing electrode. Characterization of EGOFET devices allows us to quantify the current difference at each gate voltage, as modulated by the number of target nucleotides hybridized on the sensing gate surface. This number is correlated to the molar concentration of the target analyte [T].

Complementary information was then obtained by Surface Plasmon Resonance Imaging (SPRI) performed on the same oligonucleotide pair. There, the change in refractive index (SPRI) is correlated to the functionalization and the hybridization reaction. This provides an independent assessment of the surface coverage and hybridization efficiency of the sensing gate electrode of the EGOFET sensor.

RESULTS AND DISCUSSION

EGOFET in dual gate configuration

We describe first the architecture of the dual gate EGOFET designed for miRNA sensing (Fig.1). The electrode G1 is a gold wire functionalized with 2-Mercaptoethanol (ME) monolayer, while the electrode G2 is a gold wire, symmetric to G1 with respect to the channel, functionalized with the thiolated probe P. The sequence of P was synthesized according to a sequence reported for human miRNA-21-5p (miRbase.org, 2020). According to our protocol, before the EGOFET operations, G2 is incubated in buffer solutions spiked with different target concentrations [T]. The incubation protocol is described in the *Experimental Section*. In Fig. 1a we schematically depict

the hybridization of the probes P grafted to G2 with the target analyte T. The electrode G2 is then immersed together with G1 in the buffer electrolyte of the device that comprises an organic semiconductor channel patterned on polyimide substrate (Kapton™, 50 μm) (Fig. 1b). The aqueous electrolyte is contained in a polydimethylsiloxane (PDMS) reservoir. Fig. 1c shows optical images at two different magnifications of the semiconductor channel. In particular, the optical micrograph in polarized light reveals the presence of large crystalline domains across the channel. The functionalization steps of the gate electrodes are assessed by both SPR and the electrical characterization of each EGOFET before and after each step. Details on the fabrication procedure and functionalization steps are provided in the *Experimental Section*.

The stage holder with gate electrodes (Fig. 1c) was removed from the electrolyte reservoir and electrode G2 was incubated in vials each containing different concentrations of T, starting from 10 pM to 300 pM.

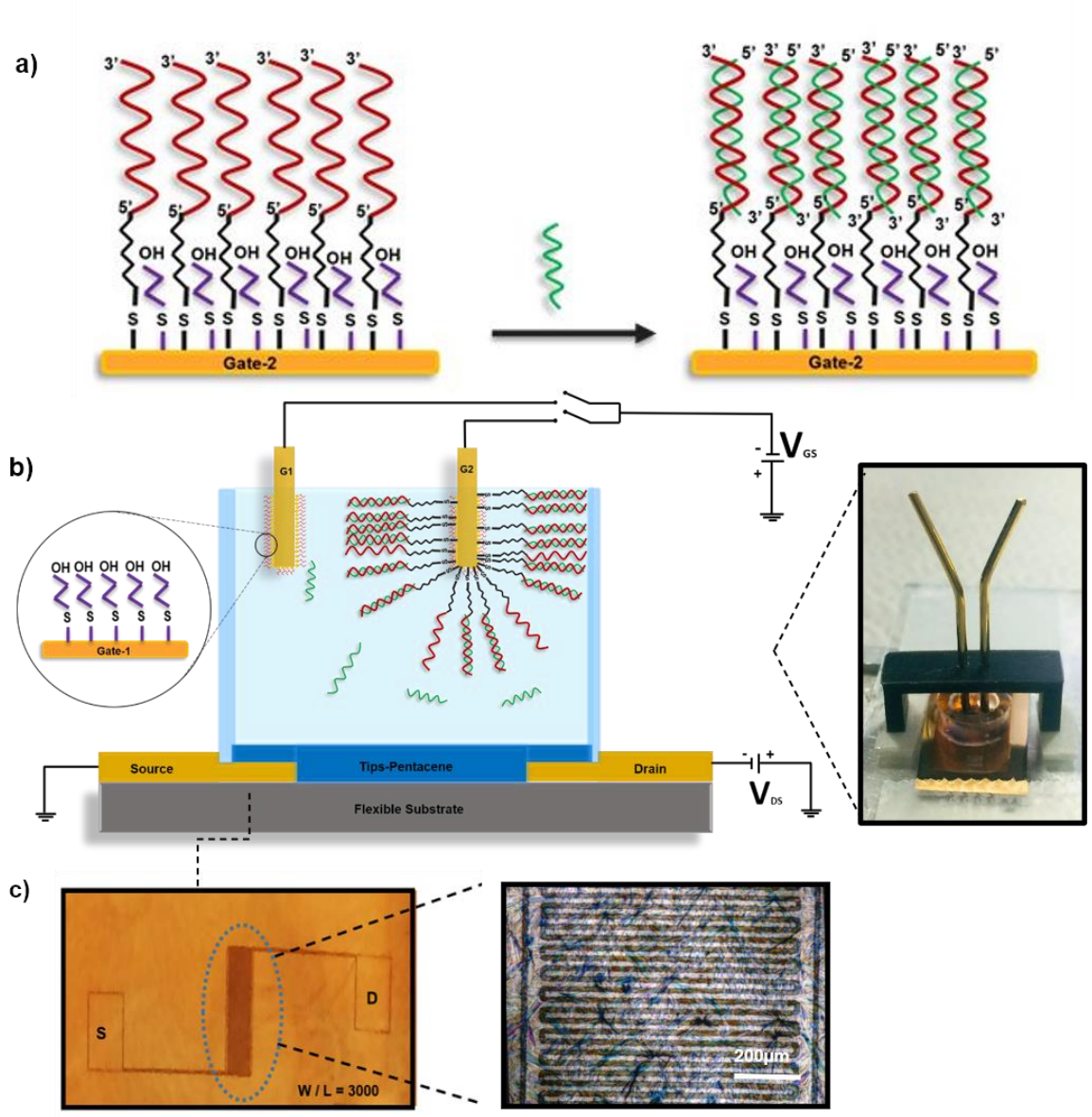

Figure 1: Functionalization of a) G2 with probe and 2-ME (left) and the hybridization process of the target analytes with G2 after incubation (right). b) Schematic drawing illustrating the architecture of the dual-gate EGOFET device featuring the PDMS microfluidics pool sealed on top of the Source and Drain interdigitated electrodes covered with TIPS-pentacene. c) Morphology of EGOFET showing a detail of the test pattern with interdigitated electrodes and contact pads, a polarized light microscopy image (10x objective) evidencing the crystals in the channel formed by TIPS-pentacene thin film.

EGOFET after hybridization.

Transfer curves of the device were obtained by measuring channel current (I_{DS}) upon sweeping Gate-Source voltages in the range from -0.2V to -0.9V with steps of -1 mV at a fixed Drain-Source voltage V_{DS}=-0.2 V. The transfer curves of the EGOFET are acquired first by sweeping the voltage bias of reference G1, while leaving sensing G2 floating. Then, within two minutes, they were acquired by sweeping the voltage bias of sensing G2, while leaving G1 floating. The values of both Drain-Source and Gate-Source currents were acquired to ensure that no short-circuit or faradaic process occurred. In order to evaluate the precision and reproducibility of the measurement performed with EGOFET, the laser ablation of the interdigitated electrodes and the deposition of the organic semiconductor upon the transistor channel were repeated for each experiment.

Fig. 2a shows an example of transfer curves recorded with G1 and G2 at different concentration [T]. The extent of residual leakage current was less than 30 nA, compared to the on-current measured in the range of 0.1 to 1 μA. We recall that only G2 was previously incubated in a buffer solution spiked with the target analyte at concentration [T]. The transfer curves for the G2 gate sweeps $I_{DS}([T], V_{GS})_{G2}$ show a decrease of current with increasing concentration [T]. Conversely, the transfer curves (dashed lines) $I_{DS}([T], V_{GS})_{G1}$ are narrowly distributed around a central value of the buffer transfer curve $I_{DS}(0, V_{GS})_{G1}$. The first evidence suggests a sizable change in the charge distribution in the proximity of the gold surface of G2 is induced by the formed hybridized complex, with respect to the single-stranded oligonucleotide. This is not observed in the case of G1. Indeed, the transfer characteristics acquired by sweeping G1 after the incubation of G2 in the target analyte solution exhibit modest fluctuations with respect to the curve recorded with the pure buffer solution, [T]=0. We ascribe these fluctuations to unspecific adsorption of target molecules on G1 during measurement, that may detach from G2 and diffuse through the solution. This process is depicted in the zoom of Fig. 1b. The scarce sensitivity of the electrode G1 to [T] enables us to assume that the transfer curves driven by G1 are independent on [T] in the range of [T] explored, viz. $\langle I_{DS}([T], V_{GS})\rangle_{G1} \approx \langle I_{DS}(V_{GS})\rangle_{G1}$.

Mean transfer curves are estimated as the logarithmic mean of N=10 measurements for each concentration by sweeping G2, and N=15 measurements for each concentration by sweeping G1:

$$\langle I_{DS}([T], V_{GS})\rangle_{G2} = 1A \cdot \langle e^{\ln[I_{DS}([T],V_{GS})/1A]}\rangle_{G2} \approx 1A \cdot e^{\langle \ln[I_{DS}([T],V_{GS})/1A]\rangle_{G2}} \quad (1a)$$

$$\langle I_{DS}([T], V_{GS})\rangle_{G1} = 1A \cdot \langle e^{\ln[I_{DS}([T],V_{GS})/1A]}\rangle_{G1} \approx 1A \cdot e^{\langle \ln[I_{DS}(V_{GS})/1A]\rangle_{G1}} \approx \langle I_{DS}(V_{GS})\rangle_{G1} \quad (1b)$$

Here the pre-factor imparts the physical dimension, and the exponent of the right equation is the logarithmic mean:

$$\langle \ln[I_{DS}([T], V_{GS})/1A]\rangle = \frac{1}{N}\sum_{i=1}^{N} \ln\left[I_{DS,i}([T], V_{GS})/1A\right] \quad (2)$$

The experimental error is estimated as:

$$\frac{\delta I_{DS}}{\langle I_{DS}\rangle} \approx \sqrt{\frac{1}{N-1}\sum_{i=1}^{N}(\ln(I_{DS}/1A) - \langle \ln(I_{DS}/1A)\rangle^2} \quad (3)$$

This procedure to calculate the mean is motivated by the transfer curve spanning by orders of magnitude in the small V_{GS} range of operations: since the arithmetic mean will wash out small features because the largest transfer curve overwhelms the others, even if it were an outlier, it is preferred to adopt the logarithmic mean as detailed previously (Parkula et al., 2020)

The logarithmic mean transfer curves, estimated from three devices each, are shown in Figure 2b with G1 (orange) and G2 (colors, each representing one concentration). The error is depicted by the corresponding color shades, and as also clear from eq. 3 increases with the current, hence with applied V_{GS}.

The transfer curves in Fig. 2a and b are recorded for hybridization with the target miRNA-21 solution. The measurement protocol is set to acquire the transfer curves mostly in the linear regime $|V_{DS}| << |V_{GS} - V_{Th}|$ that can be described according to the equation:

$$I_{DS}([T], V_{GS}) = g_m([T], V_{DS}) \cdot [V_{GS} - V_{Th}([T])]. \quad (4)$$

Here, g_m is the transconductance that depends linearly on both V_{DS} and W/L, where W and L are the channel width and length, respectively. V_{DS} and W/L are kept fixed. The threshold voltage V_{Th} represents the internal field to overcome for turning the device on. Both transconductance and threshold voltage are, in principle, sensitive to the interaction between P and T, and hence to [T]. In particular hybridization, that affects the surface potential of the gate G2, is reflected in the threshold voltage shift, and may also appear in g_m as the density of states may be changed. The

inset in Fig. 2a shows the transfer curves for hybridization with unrelated miRNA-141 (mismatched sequence is reported in the Experimental Section). The I_{DS} vs V_{GS} curve for [miRNA-14=300 pM is not significantly different from those obtained with the pristine G2 probe, whereas miRNA-21 modulates sensibly the current with concentration.

In the inset of Fig. 2b we show the threshold voltage and the transconductance extracted from the mean transfer curves $\langle I_{DS}([T], V_{GS})\rangle_{G2}$ by applying the linear fit eq. 4. We observe a logarithmic decay of $V_{Th,G2}$ vs [T]. On the other hand, we notice that the slope of the linear region of the transfer curves in Fig. 2b does not change substantially even when the curves are progressively offset towards more negative voltage values with increasing concentration. This is evidenced by the transconductance values in Fig. 2b right axis that exhibits a substantial invariance vs [T]. The presence of the negatively charged hybridized probe/target pair on the sensing gate explains both the absence of change in transconductance and the shift of the V_{TH} to more negative voltages. The more negative hybridized sensing layer induces a positive image charge on the electrode surface, thus making the gate electrode potential less negative.

In order to experimentally minimize the device-to-device variations, it is convenient referring the changes in the transfer curves to the mean curve of the reference electrode G1, the latter being largely insensitive to [T]. Therefore, we combine the transfer curves $\langle I_{DS}([T], V_{GS}\rangle_{G2}$ (obtained by sweeping the voltage at the sensing electrode G2), with $\langle I_{DS}(V_{GS})\rangle_{G1}$ (obtained by sweeping the voltage the reference electrode G1) to yield the signal S_{ref}:

$$S_{ref}([\mathrm{T}], V_{GS}) = 1 - \frac{\langle I_{DS}([\mathrm{T}], V_{GS})\rangle_{G2}}{\langle I_{DS}(V_{GS})\rangle_{G1}} \quad (5a)$$

Similarly, in order to model the dose curve later, we define the signal *S* referred to G2 as:

$$S([\mathrm{T}], V_{GS}) = 1 - \frac{\langle I_{DS}([\mathrm{T}], V_{GS})\rangle_{G2}}{\langle I_{DS}(0, V_{GS})\rangle_{G2}} \quad (5b)$$

The brackets indicate the averaging process of the transfer curves that is described in the previous section. The definition imposes a relation between *S* and S_{ref} in terms of $A(V_{GS}) = \frac{\langle I_{DS}(V_{GS})\rangle_{G1}}{\langle I_{DS}(0, V_{GS})\rangle_{G2}}$:

$$S([\mathrm{T}], V_{GS}) = [1 - A(V_{GS})] + S_{ref}([\mathrm{T}], V_{GS}) \cdot A(V_{GS}) \qquad (6)$$

Thus, the signal S_{ref} measured with respect to the reference electrode must be both rescaled and offset to be reconducted to the signal recorded with the gate G2 alone. The error δS on the signal is estimated by error propagation starting from the error eq. 3:

$$\delta S([\mathrm{T}], V_{GS}) = \delta A(V_{GS})\left[1 + S_{ref}([\mathrm{T}], V_{GS})\right] + A(V_{GS}) \cdot \delta S_{ref}([\mathrm{T}], V_{GS}) \qquad (7a)$$

$$\delta S([\mathrm{T}], V_{GS}) = \left\{\frac{\delta\langle I_{DS}\rangle_{G1}}{\langle I_{DS}\rangle_{G1}} + \frac{\delta\langle I_{DS}\rangle_{G2}}{\langle I_{DS}\rangle_{G2}}\right\} \cdot A(V_{GS})\left[1 + S_{ref}([\mathrm{T}], V_{GS})\right] + A(V_{GS}) \cdot \left[1 - S_{ref}([\mathrm{T}], V_{GS})\right] \cdot \left\{\frac{\delta\langle I_{DS}([\mathrm{T}], V_{GS})\rangle_{G2}}{\langle I_{DS}([\mathrm{T}], V_{GS})\rangle_{G2}} + \frac{\delta\langle I_{DS}\rangle_{G1}}{\langle I_{DS}\rangle_{G1}}\right\} \approx 2 \cdot A(V_{GS}) \cdot \left\{\frac{\delta\langle I_{DS}([\mathrm{T}], V_{GS})\rangle_{G2}}{\langle I_{DS}([\mathrm{T}], V_{GS})\rangle_{G2}} + \frac{\delta\langle I_{DS}\rangle_{G1}}{\langle I_{DS}\rangle_{G1}}\right\} \qquad (7b)$$

The assumption in eq. 7b is that the relative errors of the transfer curves acquired upon G2 sweeping are comparable. In eq. 7b we omitted the dependence of V_{GS} for sake of brevity.

The dose curves shown in Fig. 2c compare S_{ref} and the signal S from eq. 6 vs [T] both acquired at V_{GS}=-0.6, -0.7, -0.8 V. The signal S slows down at concentrations approaching 300 pM. We estimate, based on the transfer curves and the error width obtained from 20 experiments, that the sensitivity of the biosensor is below 50 pM, with a LOD taken to be the value of concentration corresponding to $S = 3 \cdot \delta S([0], V_{Gs})$ in the fit reported in Fig. 2c. The LOD is equal to 35 pM for gate voltages below -0.75 C (inset Fig. 2c), while the LOD increases and the sensitivity (slope) decreases as V_{GS} becomes more negative (see the curves in Fig. 2c).

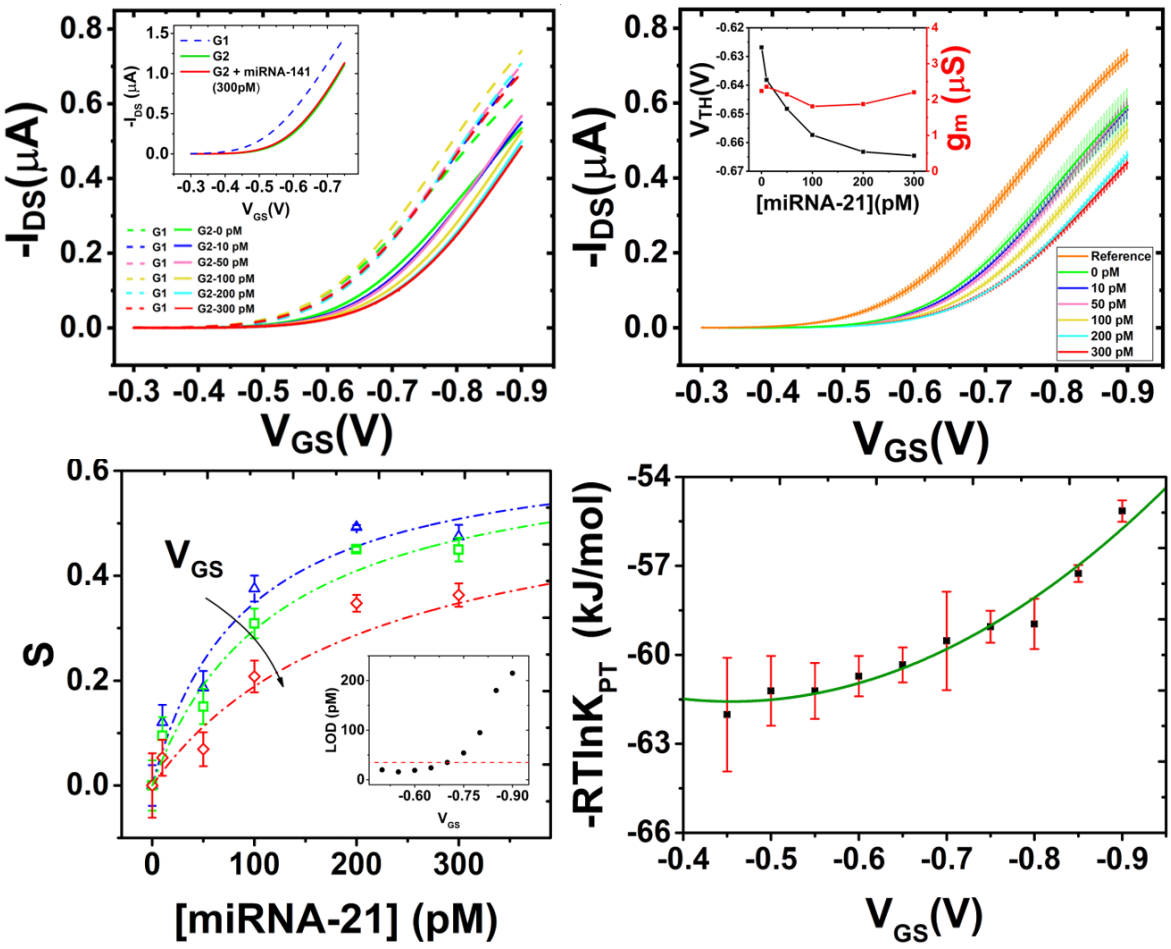

Figure 2: a) Transfer curves of EGOFET device with two-gate electrodes, characterized after incubation of both gates with solutions containing different concentrations of the target analyte; the solid lines obtained with G2 are markedly separated from the dashed curves obtained with G1 Transfer characteristics with G1 are plotted with the same color of G2 to indicate the measurement taken few minutes after G2. The response of the device to 300 pM concentrated miRNA-141 solution is plotted in the inset, confirming the selectivity of the probe. b) Plot of the logarithmic average of the transfer curves of G1 and G2 showing clear, distinct trends with statistical error. In the inset the decay of G2 threshold voltage is depicted with transconductance values reported to be almost constant at varying target concentration, c) Fitting of the dose curves calculated at three different V_{GS} (-0.6 *blue*, -0.7 *green*, -0.8 *red*) V using eq. 18; inset, plot of LOD vs V_{GS}, extracted from the fitting curve value corresponding to three times the error reported for measurements without the target analyte (dashed line indicating the value of 35 pM as maximum for $V_{GS} \geq$-0.7 V. d) Gate–voltage dependent affinity constant K_{PT} extracted from all dose curves; green continuous line is the best fit from equation (23c).

Thermodynamics of the biorecognition events.

We derive now an analytical function that describes the dose curves as in Fig. 2c for the dual gate device. The aim is not only to devise an invertible function for the dose curve, but to derive it from a chemical model that enables us to understand how biorecognition is translated into the device response. In doing this, we assume that the device (system) is in quasi-equilibrium conditions, thus we neglect this time kinetic effects. Thus, we draw the different equilibria that characterize our system, and we envision four relevant equilibria.

We start from G2 that is functionalized with the probe P, whose activity (that we take equal to concentration) is termed p_0. G2 is first incubated in the solution containing the target T at initial concentration t_0, then a first equilibrium (hybridization on the G2 electrode surface) is attained:

$$P + T \rightleftharpoons PT \qquad (8)$$

Here PT is the probe-target pair concentration whose equilibrium constant K_{PT} is the binding association constant on the electrode:

$$K_{PT} = \frac{[PT]}{[P][T]} = \frac{[PT]}{(p_0 - [PT])[T]} = \frac{(p_0 - [P])}{[P][T]} \qquad (9a)$$

$$K_{PT} = \frac{x_{eq}}{(1 - x_{eq})(t_0 - x_{eq} \cdot p_0)} = \frac{x_{eq}}{(1 - x_{eq})(1 - x_{eq} \cdot p_0 / t_0) \cdot t_0} \qquad (9b)$$

Here, $[T]$ is the concentration of target in solution, $[P]$ concentration of the free probe on the electrode, and $x_{eq} = [PT]/p_0$ is the equilibrium fraction of the hybridized probe. Langmuir modelling described the behaviour of DNA and RNA sensors based on fluorescence or electrochemistry, although the hybridization process may involve multiple reactions in competition with detection and characteristic reaction kinetics may also be regulated by hindrance effects between target and probe oligonucleotides or by the presence of the surface itself. (Halperin et al., 2006). The signal $S([T])$, dependence on x_{eq} can be described as in the Langmuir isotherm:

$$S = S_{max} x_{eq} = S_{max} \frac{K_{PT} \cdot [T]}{1 + K_{PT} \cdot [T]} \qquad (10)$$

We record the signal after the electrode G2 has equilibrated in the buffer solution of the device. Hence we write the other equilibria involving G2 and the buffer solution:

$$P \rightleftharpoons C \qquad (11a)$$

$$T + C \rightleftharpoons TC \qquad (11b)$$

$$PT \rightleftharpoons TC \qquad (11c)$$

that represent, respectively, the desorption of probe from the electrode surface (eq. 11a), the recognition between probe and target in the bulk solution (eq. 11b) where *C* is the probe that in limited amount has desorbed from the gate surface and diffuses nearby the surface free in solution, and *TC* accounts for the desorption of probe/target from the electrode surface (11c). The respective equilibrium constants are:

$$K_{des} = \frac{[C]}{[P]} \qquad (12a)$$

$$K_a = \frac{[TC]}{[C][T]} \qquad (12b)$$

$$K_{det} = \frac{[TC]}{[PT]} \qquad (12c)$$

That represent respectively the desorption constant (12a), the binding association constant in solution (12b), and the detachment constant that leads to a partition of the associated pair between electrode and solution. Mass conservation imposes that:

$$[C] + [TC] + [P] = p_0 \qquad (13a)$$

$$[T] + [TC] + [PT] = t_0 \qquad (13b)$$

By multiplying eq. 12a and eq. 12b, dividing them by eq. 12c and comparing to eq. 9, we establish the relationship among the four constants:

$$\frac{K_a K_{des}}{K_{PT}} = K_{det} \tag{14}$$

We express $[C]$ from eq. 12a, $[TC]$ from eq. 12b, then we obtain:

$$[P] = \frac{p_0}{1+K_{des}+K_a K_{des}[T]} \tag{15a}$$

$$[T] = \left\{1 + \frac{K_{PT}+K_a K_{des}}{1+K_{des}+K_a K_{des}[T]} p_0\right\}^{-1} t_0 \tag{15b}$$

Upon simplification, eq. 15b yields the second order equation:

$$K_a K_{des}[T]^2 + [T]\{1 + K_{des} + (K_{PT} + K_a K_{des})p_0 - K_a K_{des} t_0\} - \{K_{des} + 1\}t_0 = 0 \tag{16}$$

Expressed also in terms of K_{det}

$$K_a K_{des}[T]^2 + [T]\left\{1 + K_{des} + K_a K_{des}\left(1 + \frac{1}{K_{det}}\right)p_0 - K_a K_{des} t_0\right\} - \{K_{des} + 1\}t_0 = 0 \tag{17}$$

Finally, if we solve for [T] and we plug it into eq. 10, we obtain the analytical function describing the signal $S([T])$:

$$S = S_{max} \frac{K_{PT}\cdot[(K_{PT}+K_a K_{des})p_0+1]\cdot(\sqrt{W t_0+1}-1)}{K_{PT}\cdot[(K_{PT}+K_a K_{des})p_0+1](\sqrt{W t_0+1}-1)+2K_a K_{des}} \tag{18}$$

where we indicate $W = \frac{4K_a K_{des}}{[(K_{PT}+K_a K_{des})p_0+1]^2}$ to simplify notation.

We notice from eq. 18 that *S* scales as $\sqrt{t_0}$ when $W \cdot t_0 \gg 1$, thus recovering the Hill-type power law dependence shown by. (Halperin et al., 2006):

$$S \approx S_{max} \frac{\left\{\frac{2K_{PT}\sqrt{K_a K_{des}}}{[(K_{PT}+K_a K_{des})p_0+1]}\right\}\cdot\sqrt{t_0}}{1+\left\{\frac{2K_{PT}\sqrt{K_a K_{des}}}{[(K_{PT}+K_a K_{des})p_0+1]}\right\}\cdot\sqrt{t_0}} = S_{max}\frac{K_{1/2}\cdot\sqrt{t_0}}{1+K_{1/2}\cdot\sqrt{t_0}} \tag{19}$$

Instead, S scales linearly with t_0, hence recovering a Langmuir type dependence, when $W \cdot t_0 \ll 1$:

$$S \approx S_{max} \frac{\left\{\frac{2K_{PT}K_aK_{des}}{[(K_{PT}+K_aK_{des})p_0+1]}\right\}\cdot t_0}{1+\left\{\frac{2K_{PT}K_aK_{des}}{[(K_{PT}+K_aK_{des})p_0+1]}\right\}\cdot t_0} \approx S_{max} \frac{\left\{\frac{2K_{PT}K_aK_{des}}{[K_{PT}p_0+1]}\right\}\cdot t_0}{1+\left\{\frac{2K_{PT}K_aK_{des}}{[K_{PT}p_0+1]}\right\}\cdot t_0} \approx S_{max} \frac{K_1 \cdot t_0}{1+K_1 \cdot t_0} \quad (20)$$

Thus, our simple model predicts these two important cases as limit behaviors. Hence, we used the generalized Langmuir isotherm function (18) to fit the dose curve of the EGOFET biosensor. The only free fitting parameter is the equilibrium constant K_{PT}, whereas the other parameters S_{max}, K_a, K_{des}, and p_0 were fixed. In particular, K_a=1.15 10^{17} is calculated from the interaction between miRNA sequences same of P and T in solution from software DINAMELT (Markham and Zuker, 2005). K_{des} was arbitrarily fixed at 10^{-15} to indicate that it is strongly unlikely, S_{max} =0.65 and p_0=30 pM. From the analysis of experimental signal data retrieved from EGOFET current output, we obtain the value for the binding constants, for instance at V_{GS}= -0.75 V as in the plot of Fig. 2c is equal to $K_{PT} = 8.8\times10^9 \pm 1.8\times10^9$. Similarly, fitting of data was applied to all the dose plots starting from V_{GS}=-0.5V to V_{GS}=-0.9V. This allows us to analyze the dependence of the binding constant with respect to the values of gate voltage. From the values of K_{PT} obtained by best fit with eq. 18, we plot the data in Fig. 2d, keeping the temperature equal to 37°C (as in the incubation phase). We observe a non-linear monotonic trend of K_{PT} vsV_{GS}, that we interpret according to the combination of free energy of hybridization and electrostatic free energy contributions, as detailed in the following.

Calculation of free energy from EGOFET characteristics

The equilibrium constant K_{PT} is related to the molar free energy of hybridization at the G2 electrode (ΔG_0) and the electrostatic free energy (ΔG_e), according to the following factor expression:

$$K_{PT}(V_{GS}) = e^{-\frac{\Delta G_0}{RT}} \cdot \Delta e^{-\frac{\Delta G_e}{RT}} \quad (21)$$

Where R is the gas constant and T is the absolute temperature. When we expand the enthalpic part of ΔG_e at the second order, we obtain

$$\Delta G_e = \delta Q_{\text{eff}} \cdot (V_{\text{GS}} - V_0) + \delta C_{\text{eff}} \cdot (V_{\text{GS}} - V_0)^2 \quad (22)$$

The terms δQ_{eff} and δC_{eff} represent the variation of the effective charge and effective capacitance respectively, while the voltage V_0 annihilates the electrostatic free energy contribution eq. 22. In the present work V_0 has been selected equal to the minimum V_{GS} resulting from the fitting, as explained further.

By expanding equations (21) and (22) we get:

$$-RT \cdot \ln K_{PT} = \Delta G_0 + \delta Q_{\text{eff}} \cdot (V_{\text{GS}} - V_0) + \delta C_{\text{eff}} \cdot (V_{\text{GS}} - V_0)^2 \quad (23a)$$

and by grouping, we obtain the fitting function:

$$-RT \cdot \ln K_{PT} = \left(\Delta G_0 - \delta Q_{\text{eff}} V_0 + \delta C_{\text{eff}} {V_0}^2\right) + (\delta Q_{\text{eff}} - 2\delta C_{\text{eff}})\, V_{\text{GS}} + \delta C_{\text{eff}} \cdot {V_{\text{GS}}}^2 \quad (23b)$$

$$-RT \cdot \ln K_{PT} = A + B\, V_{\text{GS}} + C\, {V_{\text{GS}}}^2 \quad (23c)$$

Upon the binding of probe-target, the contribution due to the changes of the surface charge and of the surface dipole moment is represented by the linear term *B* in equation (23)). The quadratic term *C* is the change of capacitance δC_{eff} and includes both the change of interfacial capacitance between electrolyte and the gate electrode and the change of polarizability upon hybridization.

We fit the data in Fig. 2d with the parabolic equation (23c), then we extract the values of the physical properties from the best fit values *A*, *B*, and *C*. These are summarized in Table 1.

Table 1 Best fitting parameters obtained from eq.23c and the corresponding thermodynamics properties ΔG_0 and δQ_{eff} derived from eq.23b.

A (kJ/mol)	*B* (kC/mol)	$C = \delta C_{eff}$(kF/mol)	ΔG_0(kJ/mol)	δQ_{eff}(kC/mol)
-55.48±3.8	25.77±11.57	29.42±8.51	-83.3	54.77

Binding free energy was thus obtained as function of voltage. We find V_0=-0.45 V as the value of V_{GS} that zeroes the derivative of eq. 23c. We then extract ΔG_0 =-83.3kJ/mol. ΔG_0 was then compared with the binding energy generated by the simulation software DINAMELT (Markham and Zuker, 2005) for the sequences of probe and target described in the experimental section. The value of ΔG_0 calculated for the bulk reaction, according to (SantaLucia and Hicks, 2004), is -101.2 kJ/mol. We infer that our ΔG_0 value in Table 1 for the G2 electrode is comparable with respect to

the binding constant in solution. The value extracted from our EGOFET measurement is approximately 20% lower and this reduced value hints to a reduced efficiency of hybridization because of spatial confinement, as it is also supported by the SPR experiments described below.

We obtained the electrostatic free energy at V_{GS} = -0.75V equal to -13.52kJ/mol from eq. 22. The capacitive contribution to ΔGe is 0.05kJ+/mol at V_{GS} = -0.5V and increases as a power law with the drain-source voltage up to 5.8kJ/mol at V_{GS} = -0.9V. The charge contribution is dominant in the electrostatic free energy and shows a linear dependency with the applied gate-source voltage (from -2.4kJ/mol to -24.26kJ/mol at V_{GS}=-0.9V). The primary role of charge could be related to the presence of the negatively charged phosphate groups on the target RNA filaments, as observed also from the V_{TH} trend.

Impedance spectroscopy

Electrochemical experiments were performed to further validate the presence of probe on the G2 gate after the functionalization and to monitor the stability of the biorecognition layer after the incubation with blocking agent mercaptoethanol. The response of the functionalized gate towards electron transfer (between gold electrode and the redox couple $[Fe(CN)_6]^{3-/4-}$) was measured using KCl as support electrolyte (see Experimental section). Impedance spectra in faradaic regime is reported in Fig 3A for G2. From the fit relative to the Nyquist plot, the charge transfer resistance undergoes an increase after functionalization with thiolated probe nucleotide equal to approximately 1.3 kΩ and a further increase of 2kΩ after incubation with mercaptoethanol. Impedance was capable of detecting the presence of a hybridized probe-target system for a concentration of 300 pM target miRNA but was not sufficiently sensitive for a lower concentration. The $[Fe(CN)_6]^{3-/4-}$ ions might interfere with the formation and stability of the duplex, therefore the hybridization reaction was performed in a separate incubation volume, and the gate was later transferred to the electrolyte for current/voltage measurement. More importantly, impedance was used to clarify the stability of the probe functionalization for perturbation of the equilibrium between the probe and blocking agent occurring in the thermal step of hybridization. From the plot reported in Fig. 3B it is possible to appreciate a slight decrease of the imaginary part of impedance for the probe functionalized G2 after incubation at 37 °C in a solution containing just Tris-EDTA-NaCl buffer. The detached probe might be transferred in solution and be responsible for a

competitive target-probe reaction affecting the sensitivity of the biosensor as reported in previous calculation of free energy.

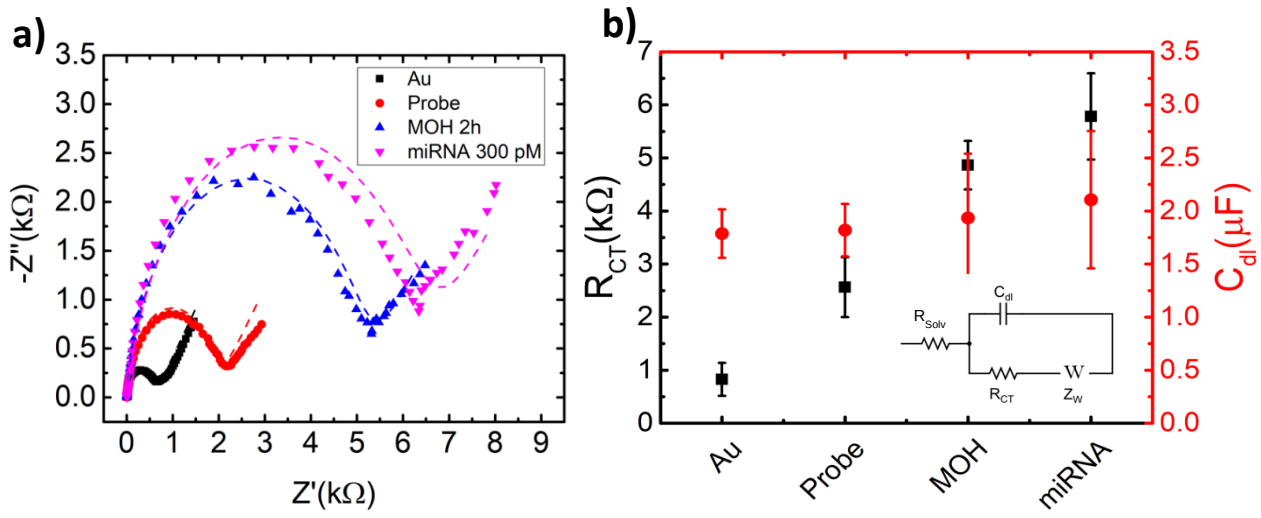

Figure 3: a) Nyquist plot characterizing the impedance of gate G2 taken on a clean gold surface (black), after the immobilization of the probe sequence obtained with thiol bonding (red), after the reaction with mercaptoethanol (blue) which is filling the available site left uncovered by the probe. The incubation with complementary miRNA-21 derived sequence is further increasing both the real and imaginary part of impedance (pink). b) Resistance to the charge transfer and Capacitance of the double layer obtained by fitting a classic Randles circuit (shown in the inset) on the Nyquist plots for the consecutive functionalization steps.

Surface plasmon resonance

We used surface plasmon resonance to obtain independent evidence of the interaction between probe and miRNA-21 target analyte. With this aim, we immobilized probe on the gold surface of the SPR sensor through direct interaction between the thiol moiety available in the structure of probe and the gold surface. Figure 4a shows a representative SPR sensorgram for the probe immobilization. The linear time-dependence of the signal detected during the adsorption of the probe is a consequence of mass-transport limited kinetics for the adsorption process.

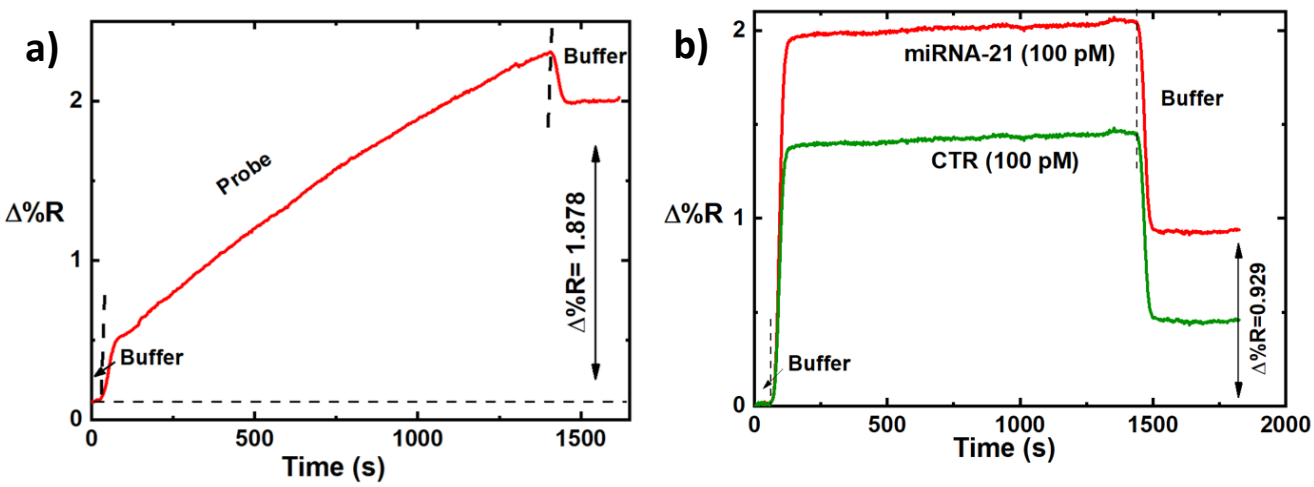

Figure 4**:** a) Representative changes in percent reflectivity (Δ%R) over time detected for the immobilization of the probe. The probe was immobilized through direct interaction of thiol moiety with the gold surface. The signal detected when the running buffer baseline was established after probe adsorption, allowed us to quantify the surface coverage of probe adsorbed on the surface corresponding to 4.7 10^{12} molecules cm^{-2}. b) Δ%R over time detected for the parallel adsorption of 100 pM solutions of miRNA-21 target analyte and CTR (unrelated control sequence) on the surface immobilized probe.

We quantified the surface coverage of probe adsorbed on the surface (4.7 10^{12} molecules cm^{-2}) measuring the variation of the detected signal after the adsorption of the probe (Δ%R=1.878). The number of molecules per unit area was estimated on the basis of the theoretical model described by Shumaker-Parry et al. (Shumaker-Parry and Campbell, 2004)

Figure 4b shows representative SPR sensorgram detected for the hybridization of target analyte (miRNA-21) and the interaction of the control unrelated sequence (CTR). Both experiments were conducted using 100 pM solutions. The larger SPR shift detected for the interaction between miRNA-21 and target provided evidence of the capacity of the probe to interact with the miRNA-21 target sequence preferentially.

SPR data referring to the probe immobilization and target hybridization allowed us to calculate the hybridization efficiency (HE) as $HE = (\Delta\%R_{hybridization} \cdot MW_{Probe} / \Delta\%R_{immobilization} \cdot MW_{miRNA\text{-}21})$ where MW_{Probe} and $MW_{miRNA\text{-}21}$ correspond to the molecular weight of the probe and miRNA-21, respectively. HE represents the ratio of probes immobilized on the gold surface that formed a

duplex with the target sequence (Špringer et al., 2010). HE=0.69 was obtained for the interaction of the probe with 100pM miRNA-21 target analyte, thus demonstrating the capacity of the surface-immobilized probe to catch low concentrated miRNA-21 target molecules.

Conclusions

We demonstrated that EGOFET biosensors are suitable label free devices for recognition of short sequences of genetic materials in the picomolar region. The oligomer miRNA-21 was selected as a relevant prototype to study the capability of EGOFET to detect the formation of probe-target duplex in the case of an almost complementary matching. This proof of concept was achieved in a buffer suitable for hybridization and should be assessed in biological fluids. The proposed architecture features a second gate electrode working as reference for the extraction of the genuine biorecognition signal. The intrinsic shift of response due to semiconductor change of performance in liquid media is now taken into account by dual gate measurement and data analysis. Statistical analysis of the transfer curves allowed us to reconstitute the trend common to different organic transistors fabricated with simple process steps. Gate electrodes functionalized with thiolated oligonucleotide probes are biorecognition interfaces suitable for EGOFET detection scheme since the charges distributed in the oligonucleotide backbone and the stabilizing surrounding media may contribute to signal enhancement and the main mechanism of transduction is based on capacitance. The regeneration of the functionalized gate electrode, although not targeted in the present experiment, will be crucial for transfer of the technology to diagnostic assays.

The free energy of the couple probe-target was inferred by fitting the trend of the binding constant vs V_{GS} . We find a value sensibly lesser than the binding energy extracted for the homogeneous reaction in solution. This is due to the detachment of the probe and the occurrence of uncontrolled hybridization also in solution even at low concentration, and to the presence of a surface hindered hybridization reaction. The dependence of the signal with respect to square root of target concentration affects the sensitivity, which, however, is still attractive for developing multiplexed electronic biosensors for miRNA panel assays. Impedance spectroscopy measurements of the functionalized gate were used to validate the stability of the biorecognition layer positively, whereas SPR complementary detection confirmed a hybridization efficiency of 69% for the probe-target interaction. Multiplexed EGOFET biosensors with dual gate may indeed represent a viable

perspective for integrated devices for genic recognition whose data may be analyzed with good confidence and across-sample measurements. This would be very important, for instance, in the label-free detection not only of miRNA biomarkers, but also in the discrimination of point mutations of viruses and microrganisms, as it is very actual in the present epidemics.

Experimental section

Interdigitated Source (S) and Drain (D) electrodes

Source and Drain interdigitated electrodes are patterned upon a thin foil of Kapton (50 μm thickness). Physical Vapor Deposition (PVD) was accomplished by Crevac, Dresden, Germany to metallize the surface. Organic semiconductor 6,13-Bis(triisopropylsilylethynyl)pentacene (TIPS-pentacene, OSSILA) was deposited on top using simple drop casting technique. Tips- Pentacene has the ability to form a crystalline structure, contributing to efficient charge transport, however Thick crystal structures lead to the formation of small solid blocks on top of the pattern and will not passivate the complete interdigitated pattern.

Gate electrodes (G1 and G2)

Gold wires were purchased from Nanovision S.r.l, Brugherio (IT) with purity of 99.99%, a length of 2.5cm and a diameter of 1.5 mm. The gold wire has proven to be a good alternative to the classical planar / flat surface, due to the possibility to regenerate the surface with sulfuric acid cleaning procedure, and easy operation for functionalization and contact making. In order to assemble the gate electrode on top of the electrolyte and to obtain a final model, a 3D printed gate holder was designed and fabricated. Polydimethylsiloxane (PDMS) was used to generate a pool which could contain 70μl-80μl of the buffer solution and preserve contact pads from leaking buffer solution

Surface Plasmon Resonance Imaging apparatus

Gold chips for SPRI were purchased from Xantec Bioanalytics (Germany). We washed the cleaned chips with ethanol and dried them under a nitrogen stream. An SPR imager apparatus (GWC Technologies, USA) equipped with a white light source and an SF-10 prism coupled with a poly(dimethylsiloxane) microfluidic device was used for the experiments as elsewhere described. (Grasso et al., 2009). SPR image data were converted into percentage of reflectivity (%R) using the equation $\%R = 85 (I_p/I_s)$ where I_p and I_s refer to the intensity of the reflected p- and s-polarized light, respectively. We obtained kinetic data plotting the difference in %R (Δ%R) from selected regions of interest of SPR images as a function of time. We used a PDMS microfluidic device with six parallel microchannels (80 μm depth, 1.4 cm length, 400 μm width) to achieve independent control of parallel interactions occurring on the gold chip surface.

Functionalization protocol

Synthetic oligonucleotides were purchased from Metabion Internation AG, according to the following sequences:

- miRNA-21-3p derived sequence (5'- CAACACCAGUCGAUGGGCUGU- 3'), as the target analyte,
- Thiol-C6-AAA AAAA-5'- UAGCUUAUCAGACUGAUGUUGA – 3', synthetized with thiol group, C6 and 7 adenine spacers, as the probe,
- miRNA-141 derived sequence (5'-CAUCUUCCAGUACAGUGUUGGA- 3'), as the control unrelated sequence (CTR).

The stock solutions for probe and target containing segments of miRNA sequences were prepared in (sodium chloride-sodium phosphate- ethylenediaminetetraacetic acid) (SSP-EDTA) and tris(hydroxymethyl)aminomethane hydrochloride (Tris-HCl), with details reported previously (Cardoso et al., 2016). 2-mercaptoethanol (2-ME) blocking agent was selected to reduce the direct interaction between the target analyte and the gold surface. All the reagents were purchased by Merck-Sigma Aldrich.

The following gate functionalization steps were performed: 1) G1 was functionalized with 2-mercaptoethanol for the whole night at the room temperature, then rinsed with the ultrapure water before assembling; 2) G2 was functionalized with probe (2μM), for the whole night at room temperature. Later G2 was rinsed with ultrapure water and then placed in the vial containing 1mM concentration of the blocking agent (2-ME), in order to block the non-specific bindings.

Hybridization

Hybridization with the different concentrations of the target analyte was performed by incubating the G2 at 37°C for 30minutes (Bhagavan and Ha, 2015)

Electrochemical characterization

The impedance spectroscopy data were acquired by using a CH Instrument potentiostat 760c model with a three-electrodes set-up, where the gate electrode was connected as working electrode, alongside an Ag/AgCl reference electrode (Elbatech, Livorno Italy) and a Pt wire as counter electrode, all in an electrochemical cell, filled with an aqueous solution of 5 mM $K_3(FeCN_6)$, 0.1

M KCl. The impedance spectra were recorded between 0.1 Hz and 100 MHz, at a fixed potential of 0.2 V. The Nyquist plots fits were obtained with the EIS Spectrum Analyzer software.

SPRI experiments

We immobilized the probe introducing solution (0.2 μM in PBS, flow rate 10 μL min^{-1} for 30 minutes) in the microfluidic device in contact with the SPRI gold surface. After the probe immobilization and equilibration with PBS, the modified surface was passivated with 2-mercaptoethanol (1 mM in PBS) for 15 minutes.

miRNA-21 target and miRNA-141 (CTR, control scrambled sequence) solutions (100 pM in PBS + $MgCl_2$ 10 mM) were injected (10 μL min^{-1}) into parallel channels of the microfluidic device for 30 minutes. The discrimination between target and control sequences was assessed by comparing SPRI signals produced by PBS running buffer before and after target and CTR adsorption.

CRediT authorship contribution statement

Meenu Selvaraj: Investigation, Data Curation, Methodology, Writing - original draft, Writing - review & editing. **Pierpaolo Greco**: Conceptualization, Data curation, Formal analysis, Supervision, Writing - original draft, Writing - review & editing. **Matteo Sensi**: Data curation, Methodology, Supervision, Writing - review & editing. **Gulseren Deniz Saygin**: Data curation, Formal analysis, Writing - review & editing. **Noemi Bellassai**: Data Curation, Methodology, Writing - original draft. **Roberta D'Agata**: Methodology, Validation, Writing - original draft **Giuseppe Spoto**: Methodology, Validation, Supervision, Funding acquisition, Writing - review & editing. **Fabio Biscarini**: Conceptualization, Formal analysis, Modelling, Validation, Supervision, Funding acquisition, Writing - original draft, Writing - review & editing.

Declaration of competing interest

The authors declare that they have no known competing financial

interests or personal relationships that could have appeared to influence

the work reported in this paper.

Acknowledgments

This work was financially supported by the European Commission through the Marie Sklodowska-Curie ITN projects “AiPBAND” grant n.7642810 (MS, plus PG, GS, RdA, NB) and “BORGES” grant n. 813863 (DS), by the EuroNanoMed III project “AMI” (PG, MS) and by the Life Science Department of the University of Modena and Reggio Emilia, through “FAR2018” (FB)

References

Aspermair, P., Ramach, U., Reiner-Rozman, C., Fossati, S., Lechner, B., Moya, S.E., Azzaroni, O., Dostalek, J., Szunerits, S., Knoll, W., Bintinger, J., 2020. Dual Monitoring of Surface Reactions in Real Time by Combined Surface-Plasmon Resonance and Field-Effect Transistor Interrogation. J. Am. Chem. Soc. 142, 11709–11716. https://doi.org/10.1021/jacs.9b11835

Bellassai, N., D’Agata, R., Jungbluth, V., Spoto, G., 2019. Surface Plasmon Resonance for Biomarker Detection: Advances in Non-invasive Cancer Diagnosis. Front Chem 7. https://doi.org/10.3389/fchem.2019.00570

Berto, M., Casalini, S., Di Lauro, M., Marasso, S.L., Cocuzza, M., Perrone, D., Pinti, M., Cossarizza, A., Pirri, C.F., Simon, D.T., Berggren, M., Zerbetto, F., Bortolotti, C.A., Biscarini, F., 2016. Biorecognition in Organic Field Effect Transistors Biosensors: The Role of the Density of States of the Organic Semiconductor. Anal. Chem. 88, 12330–12338. https://doi.org/10.1021/acs.analchem.6b03522

Bhagavan, N.V., Ha, C.-E., 2015. Chapter 21 - Structure and Properties of DNA, in: Bhagavan, N.V., Ha, C.-E. (Eds.), Essentials of Medical Biochemistry (Second Edition). Academic Press, San Diego, pp. 381–400. https://doi.org/10.1016/B978-0-12-416687-5.00021-X

Cadoni, E., Manicardi, A., Madder, A., 2020. PNA-Based MicroRNA Detection Methodologies. Molecules 25, 1296. https://doi.org/10.3390/molecules25061296

Cardoso, A.R., Moreira, F.T.C., Fernandes, R., Sales, M.G.F., 2016. Novel and simple electrochemical biosensor monitoring attomolar levels of miRNA-155 in breast cancer. Biosensors and Bioelectronics 80, 621–630. https://doi.org/10.1016/j.bios.2016.02.035

Casalini, S., Dumitru, A.C., Leonardi, F., Bortolotti, C.A., Herruzo, E.T., Campana, A., de Oliveira, R.F., Cramer, T., Garcia, R., Biscarini, F., 2015. Multiscale Sensing of Antibody–Antigen Interactions by Organic Transistors and Single-Molecule Force Spectroscopy. ACS Nano 9, 5051–5062. https://doi.org/10.1021/acsnano.5b00136

D’Agata, R., Spoto, G., 2019. Advanced methods for microRNA biosensing: a problem-solving perspective. Anal Bioanal Chem 411, 4425–4444. https://doi.org/10.1007/s00216-019-01621-8

Fang, H., Xie, J., Zhang, M., Zhao, Z., Wan, Y., Yao, Y., 2017. miRNA-21 promotes proliferation and invasion of triple-negative breast cancer cells through targeting PTEN. Am J Transl Res 9, 953–961.

Feng, Y.-H., Tsao, C.-J., 2016. Emerging role of microRNA-21 in cancer (Review). Biomedical Reports 5, 395–402. https://doi.org/10.3892/br.2016.747

Gambari, R., Brognara, E., Spandidos, D.A., Fabbri, E., 2016. Targeting oncomiRNAs and mimicking tumor suppressor miRNAs: New trends in the development of miRNA

therapeutic strategies in oncology (Review). International Journal of Oncology 49, 5–32. https://doi.org/10.3892/ijo.2016.3503

Gasparello, J., Allegretti, M., Tremante, E., Fabbri, E., Amoreo, C.A., Romania, P., Melucci, E., Messana, K., Borgatti, M., Giacomini, P., Gambari, R., Finotti, A., 2018. Liquid biopsy in mice bearing colorectal carcinoma xenografts: gateways regulating the levels of circulating tumor DNA (ctDNA) and miRNA (ctmiRNA). Journal of Experimental & Clinical Cancer Research 37, 124. https://doi.org/10.1186/s13046-018-0788-1

Giuffrida, M.C., Zanoli, L.M., D'Agata, R., Finotti, A., Gambari, R., Spoto, G., 2015. Isothermal circular-strand-displacement polymerization of DNA and microRNA in digital microfluidic devices. Anal Bioanal Chem 407, 1533–1543. https://doi.org/10.1007/s00216-014-8405-4

Grasso, G., D'Agata, R., Zanoli, L., Spoto, G., 2009. Microfluidic networks for surface plasmon resonance imaging real-time kinetics experiments. Microchemical Journal 93, 82–86. https://doi.org/10.1016/j.microc.2009.05.001

Hakimian, F., Ghourchian, H., Hashemi, A. sadat, Arastoo, M.R., Behnam Rad, M., 2018. Ultrasensitive optical biosensor for detection of miRNA-155 using positively charged Au nanoparticles. Scientific Reports 8, 2943. https://doi.org/10.1038/s41598-018-20229-z

Halperin, A., Buhot, A., Zhulina, E.B., 2006. On the hybridization isotherms of DNA microarrays: the Langmuir model and its extensions. J. Phys.: Condens. Matter 18, S463–S490. https://doi.org/10.1088/0953-8984/18/18/S01

Khalil, S., Fabbri, E., Santangelo, A., Bezzerri, V., Cantù, C., Gennaro, G.D., Finotti, A., Ghimenton, C., Eccher, A., Dechecchi, M., Scarpa, A., Hirshman, B., Chen, C., Ferracin, M., Negrini, M., Gambari, R., Cabrini, G., 2016. miRNA array screening reveals cooperative MGMT-regulation between miR-181d-5p and miR-409-3p in glioblastoma. Oncotarget 7, 28195–28206. https://doi.org/10.18632/oncotarget.8618

Landgraf, P., Rusu, M., Sheridan, R., Sewer, A., Iovino, N., Aravin, A., Pfeffer, S., Rice, A., Kamphorst, A.O., Landthaler, M., Lin, C., Socci, N.D., Hermida, L., Fulci, V., Chiaretti, S., Foà, R., Schliwka, J., Fuchs, U., Novosel, A., Müller, R.-U., Schermer, B., Bissels, U., Inman, J., Phan, Q., Chien, M., Weir, D.B., Choksi, R., Vita, G.D., Frezzetti, D., Trompeter, H.-I., Hornung, V., Teng, G., Hartmann, G., Palkovits, M., Lauro, R.D., Wernet, P., Macino, G., Rogler, C.E., Nagle, J.W., Ju, J., Papavasiliou, F.N., Benzing, T., Lichter, P., Tam, W., Brownstein, M.J., Bosio, A., Borkhardt, A., Russo, J.J., Sander, C., Zavolan, M., Tuschl, T., 2007. A Mammalian microRNA Expression Atlas Based on Small RNA Library Sequencing. Cell 129, 1401–1414. https://doi.org/10.1016/j.cell.2007.04.040

Lauro, M.D., Buscemi, G., Bianchi, M., Salvo, A.D., Berto, M., Carli, S., Farinola, G.M., Fadiga, L., Biscarini, F., Trotta, M., undefined/ed. Photovoltage generation in enzymatic bio-hybrid architectures. MRS Advances 1–6. https://doi.org/10.1557/adv.2019.491

Lu, T.X., Munitz, A., Rothenberg, M.E., 2009. MicroRNA-21 Is Up-Regulated in Allergic Airway Inflammation and Regulates IL-12p35 Expression. The Journal of Immunology 182, 4994–5002. https://doi.org/10.4049/jimmunol.0803560

Luo, G., Luo, Wentao, Sun, X., Lin, J., Wang, M., Zhang, Yang, Luo, Weishi, Zhang, Yong, 2017. MicroRNA-21 promotes migration and invasion of glioma cells via activation of Sox2 and β-catenin signaling. Molecular Medicine Reports 15, 187–193. https://doi.org/10.3892/mmr.2016.5971

Macchia, E., Manoli, K., Di Franco, C., Picca, R.A., Österbacka, R., Palazzo, G., Torricelli, F., Scamarcio, G., Torsi, L., 2020. Organic Field-Effect Transistor Platform for Label-Free, Single-Molecule Detection of Genomic Biomarkers. ACS Sens. 5, 1822–1830. https://doi.org/10.1021/acssensors.0c00694

Majd, S.M., Salimi, A., Ghasemi, F., 2018. An ultrasensitive detection of miRNA-155 in breast cancer via direct hybridization assay using two-dimensional molybdenum disulfide field-effect transistor biosensor. Biosensors and Bioelectronics 105, 6–13. https://doi.org/10.1016/j.bios.2018.01.009

Markham, N.R., Zuker, M., 2005. DINAMelt web server for nucleic acid melting prediction. Nucleic Acids Res 33, W577–W581. https://doi.org/10.1093/nar/gki591

Markou, A., Zavridou, M., Lianidou, E.S., 2016. miRNA-21 as a novel therapeutic target in lung cancer. Lung Cancer (Auckl) 7, 19–27. https://doi.org/10.2147/LCTT.S60341

Miao, X., Wang, W., Kang, T., Liu, J., Shiu, K.-K., Leung, C.-H., Ma, D.-L., 2016. Ultrasensitive electrochemical detection of miRNA-21 by using an iridium(III) complex as catalyst. Biosensors and Bioelectronics 86, 454–458. https://doi.org/10.1016/j.bios.2016.07.001

miRbase.org, 2020. miRNA Entry for MI0000077 [WWW Document]. URL http://www.mirbase.org/cgi-bin/mirna_entry.pl?acc=MI0000077 (accessed 12.16.20).

Parkula, V., Berto, M., Diacci, C., Patrahau, B., Di Lauro, M., Kovtun, A., Liscio, A., Sensi, M., Samorì, P., Greco, P., Bortolotti, C.A., Biscarini, F., 2020. Harnessing Selectivity and Sensitivity in Electronic Biosensing: A Novel Lab-on-Chip Multigate Organic Transistor. Anal. Chem. https://doi.org/10.1021/acs.analchem.0c01655

Qu, K., Zhang, X., Lin, T., Liu, T., Wang, Zhixin, Liu, S., Zhou, L., Wei, J., Chang, H., Li, K., Wang, Zheng, Liu, C., Wu, Z., 2017. Circulating miRNA-21-5p as a diagnostic biomarker for pancreatic cancer: evidence from comprehensive miRNA expression profiling analysis and clinical validation. Scientific Reports 7, 1692. https://doi.org/10.1038/s41598-017-01904-z

SantaLucia, J., Hicks, D., 2004. The Thermodynamics of DNA Structural Motifs. Annual Review of Biophysics and Biomolecular Structure 33, 415–440. https://doi.org/10.1146/annurev.biophys.32.110601.141800

Sensi, M., Berto, M., Gentile, S., Pinti, M., Conti, A., Pellacani, G., Salvarani, C., Cossarizza, A., Bortolotti, C.A., Biscarini, F., 2020. Anti-drug antibody detection with label-free electrolyte-gated organic field-effect transistors. Chem. Commun. https://doi.org/10.1039/D0CC03399E

Shumaker-Parry, J.S., Campbell, C.T., 2004. Quantitative Methods for Spatially Resolved Adsorption/Desorption Measurements in Real Time by Surface Plasmon Resonance Microscopy. Anal. Chem. 76, 907–917. https://doi.org/10.1021/ac034962a

Špringer, T., Šípová, H., Vaisocherová, H., Štěpánek, J., Homola, J., 2010. Shielding effect of monovalent and divalent cations on solid-phase DNA hybridization: surface plasmon resonance biosensor study. Nucleic Acids Res 38, 7343–7351. https://doi.org/10.1093/nar/gkq577